Applied Catalysis B: Environmental 144 (2014) 57–65

Contents lists available at ScienceDirect

Applied Catalysis B: Environmental

journal homepage: www.elsevier.com/locate/apcatb

Single-step sensitization of reduced graphene oxide sheets and CdS nanoparticles on ZnO nanorods as visible-light photocatalysts

Rajendra C. Pawar, Caroline Sunyong Lee*

Department of Materials Engineering, Hanyang University, Ansan 426-791, Gyeonggi-do, South Korea

ARTICLE INFO

Article history:
Received 5 February 2013
Received in revised form 6 June 2013
Accepted 21 June 2013
Available online 29 June 2013

Keywords:
Reduced graphene oxide
CdS
ZnO
Photocatalysis
Chemical method

ABSTRACT

Novel composite photocatalysts composed of reduced graphene oxide (RGO) sheets, CdS nanoparticles (CNPs), and ZnO nanorods were developed using a simple low-temperature chemical approach. The RGO sheets and CNPs were sensitized via single-step chemical bath deposition at 70 °C. Because of the incorporation of RGO into the CdS and ZnO structures, the photodegradation performance toward methylene blue (MB) degradation under visible light illumination was significantly improved compared with that of just CdS and ZnO. The highest kinetic rate constant ($k = 0.028\ min^{-1}$) using 0.20 wt% of added RGO was four times higher than that without graphene. This composite degraded MB within 40 min. Such improved performance resulted from effective separation of electron-hole pairs by the RGO sheets. Photoluminescence quenching, increased optical absorbance, and high specific surface area ($23.08\ m^2\ g^{-1}$) also contributed to the high degradation efficiency. An energy level diagram was constructed to explain how the RGO sheets minimized the recombination rate. The developed RGO–CdS–ZnO composites have a potential application in water purification devices.

1. Introduction

Heterogeneous photocatalysts play crucial roles in advanced water purification devices because of their broad applicabilities and better performances compared to homogeneous catalysts [1,2]. Among the photocatalysts, ZnO has been shown to be promising because of its high electron mobility at room temperature ($155\ cm^2\ V^{-1}\ s^{-1}$), rich family of nanostructures, non-toxicity, low cost, and a bandgap that is similar to that of TiO_2 [3–6]. Despite their good performances and stabilities, ZnO-based photocatalysts have limited applications because of a wide bandgap energy (3.37 eV) and high recombination rate. Hence, various research groups have tried to improve its photocatalytic activity using different approaches such as element doping, sensitization with a visible bandgap semiconductor, and use of gold (Au) nanoparticles [7–10]. Cho et al. developed visible (VIS) and ultraviolet (UV) photocatalysts based on a ZnSe-sensitized ZnO composite [11]. Kundu et al. explored the high absorptivity of ZnO nanorods sensitized with CdS particles and showed that the particle density coverage was important for increasing photocatalytic activity [12]. Yan et al. synthesized a ZnO/TiO_2 core-brush structure and demonstrated that an interaction effect can reduce the recombination rate [13]. Han et al. compared the photocatalytic performance of ZnO nanorods and flowerlike structures and observed that the latter exhibited superior activity because of high surface areas and direct electron transport through branches [14]. Lai et al. reported that the larger oxygen vacancies in flowerlike ZnO led to a higher reaction rate and catalytic activity toward rhodamine B photodegradation [15]. Eskizeybek et al. reported an improvement in photodegradation efficiency in sunlight with ZnO nanostructures and polyaniline composites [16]. Bizarro studied Al-doped ZnO nanostructures and found that photocatalytic activity was affected by surface morphology [17]. Udawatte et al. synthesized Au/ZnO nanoparticle composites to minimize the photoelectron recombination rate [18]. However, these combinations suffered from low catalytic performance, low visible light absorptivity and stability, and high cost.

Recently, low bandgap semiconductor sensitization has been reported as the best option spanning the UV as well as the VIS portions of the solar spectrum [19,20]. A low bandgap semiconductor can potentially use multiple electron-hole pair generation per incident photon to achieve higher photocatalytic activity [21]. Various researchers have proposed visible-bandgap semiconductors for effective sensitization, such as CdSe, InP, CdTe, PbS, and CdS [22–26]. Among these sensitizers, CdS is highly promising because of its reasonable bandgap (2.42 eV), which offers new opportunities for light harvesting. Recently, our group reported CdS-sensitized ZnO nanorods synthesized using a chemical bath deposition method and their use in a solar cell application [27]. Wang et al. improved the stability and catalytic activity

* Corresponding author. Tel.: +82 2314004697.
E-mail addresses: sunyonglee@hanyang.ac.kr, sunyong523@gmail.com (C.S. Lee).

0926-3373/$ – see front matter © 2013 Elsevier B.V. All rights reserved.
http://dx.doi.org/10.1016/j.apcatb.2013.06.022

by synthesizing a CdS–ZnO core–shell structure using a modified hydrothermal method [28]. Li et al. used a simple two-step process to prepare CdS–ZnO heterostructure photocatalysts having improved performance because of low recombination rates [29]. Although these had satisfactory photodegradation performance, it was not sufficient for commercial photocatalytic devices. Improving the photocatalytic efficiency is essential by avoiding recombination losses and promoting fast electron transportation.

With the discovery of RGO, a wide range of potential applications was expected because of its remarkable properties including high electron mobility at room temperature, large theoretical specific surface area ($2630\,m^2\,g^{-1}$), excellent thermal conductivity ($3000–5000\,Wm^{-1}\,K^{-1}$), good optical transparency (97.7%), and high Young's modulus (~1 TPa) [30]. RGO has been combined with various semiconductors including ZnO, CdS, TiO_2, Fe_3O_4, SnO_2, Cu_2O, and WO_3, and its use has been explored in supercapacitors, solar cells, gas sensors, batteries, and photocatalysts [31–34]. It plays a crucial role in photocatalysis for the effective separation of photogenerated electron-hole pairs because of its electron-capturing ability [35]. RGO may also be effective for the photodegradation of water pollutants, and methylene blue (MB) dye can be used as a test pollutant. We investigated the incorporation of RGO into CNPs and ZnO nanorods for the effective photodegradation of MB dye in visible light. A unique low-temperature, water-based method for the single-step sensitization of RGO and CdS on ZnO nanorods is described in this paper.

We measured the photocatalytic performance in visible light of composites composed of RGO, CdS, and ZnO. RGO sheets and CNPs were coated onto the surface of ZnO nanorods at 70 °C. We varied the weight percentage of RGO to study its effect on the photocatalytic activity of the CNPs and ZnO nanorods. We correlated the optoelectronic properties of the composites to their photocatalytic activities. A schematic diagram describing the electron transport through the RGO–CdS–ZnO composites was constructed based on these studies.

2. Experimental details

2.1. Preparation of ZnO nanorods

ZnO nanorods were grown using an aqueous chemical process. A uniform ZnO buffer layer was deposited onto ultrasonically cleaned glass and fluorine-doped tin oxide (FTO)-coated glass substrates. The seed solution was prepared in absolute ethanol from 0.05 M zinc acetate ($Zn(CH_3COO)_2{\cdot}2H_2O$, 99.5%) and 0.05 M diethanolamine ($HN(CH_2CH_2OH)_2$, DEA, 99.5%). The clean substrate was dip-coated for 10 s in the seed solution and then dried overnight at room temperature. The dried films were annealed at 400 °C for 5 min in air to provide a buffer layer of ZnO on the substrate. This coating process was repeated twice to ensure uniform coverage. The buffer layer-coated substrate was then placed vertically in 200 mL of 0.05 M zinc acetate and 0.05 M hexamethylenetetramine (HMTA), and refluxed at 95 ± 3 °C for 5 h. This formed a coating of ZnO nanorods on the substrate.

2.2. Preparation of reduced graphene oxide

A modified Hummers method was used to prepare graphene oxide (GO) powders [36]. In brief, 2 g of graphite flakes was added to 100 mL of sulfuric acid (H_2SO_4) with constant stirring at a temperature below 10 °C. Then 8 g of potassium permanganate ($KMnO_4$) powder was gradually added at the same temperature, followed by 2 h of constant stirring. Then the mixture was stirred for 1 h at room temperature. The mixture was cooled in a low temperature bath to below 10 °C and subsequently diluted with 100 mL of distilled water. Hydrogen peroxide (H_2O_2, 30%, 20 mL) was added to the mixture to dissolve residual permanganate. A large amount of bubbles were released and the color of the mixture changed to brilliant yellow. The colored suspension was filtered and washed several times with 1 M hydrochloric acid (HCl) and distilled water. The final residue was dried in an oven at 60 °C for 12 h and stored in a vacuum oven. To reduce graphene oxide, 100 mg of GO powder was dispersed by ultrasonication for 1 h in 100 mL of distilled water. Then 20 μL of hydrazine monohydrate was added and the solution was refluxed at 90 °C for 2 h. The refluxed solution was filtered and the powder was collected in a glass Petri dish. The Petri dish containing the reduced graphene oxide was kept in an oven at 60 °C for 12 h and then then stored in a vacuum oven. The RGO powder turned black when it was dispersed using ultrasonication in distilled water as it oxidized back to graphene oxide.

2.3. Sensitization of ZnO nanorods with RGO nanosheets and CNPs

Coating of the ZnO nanorods with RGO sheets and CNPs was done in one step using a chemical bath deposition method. Initially, an optimized amount of RGO was dispersed by ultrasonication in 80 mL of distilled water over 1 h at room temperature. Then cadmium sulfate (0.005 M) and thiourea (0.005 M) were added into the graphene dispersion with stirring and the pH of the solution was adjusted to 11 using ammonia. Then, the film with the ZnO nanorods was immersed in the solution and stirred for up to 5 h at 70 °C. The substrate now coated with a film of CdS- and RGO-sensitized ZnO nanorods was removed from the bath and rinsed in

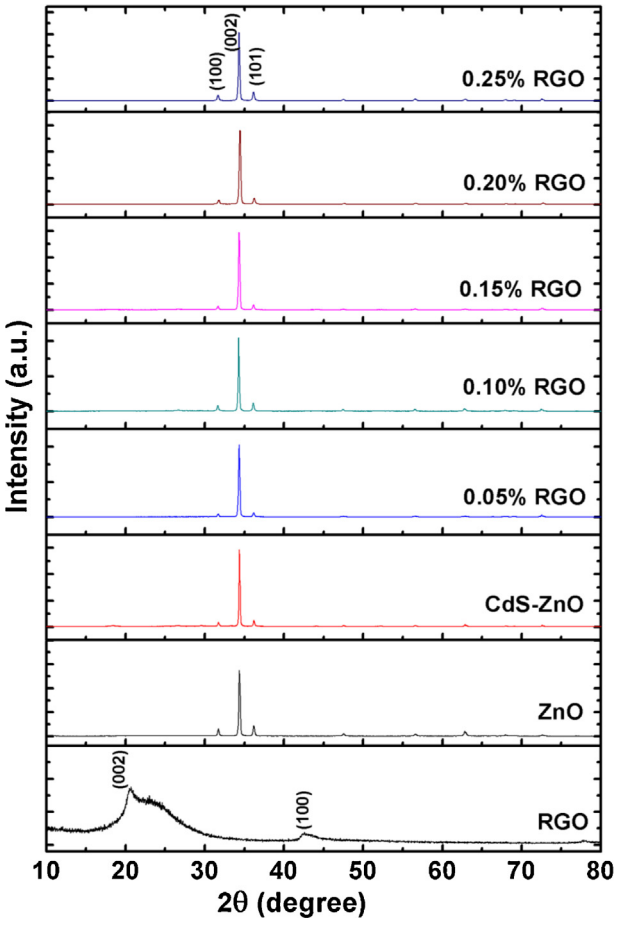

Fig. 1. XRD patterns of RGO, ZnO nanorods, CdS-sensitized ZnO nanorods, and RGO–CdS–ZnO composites.

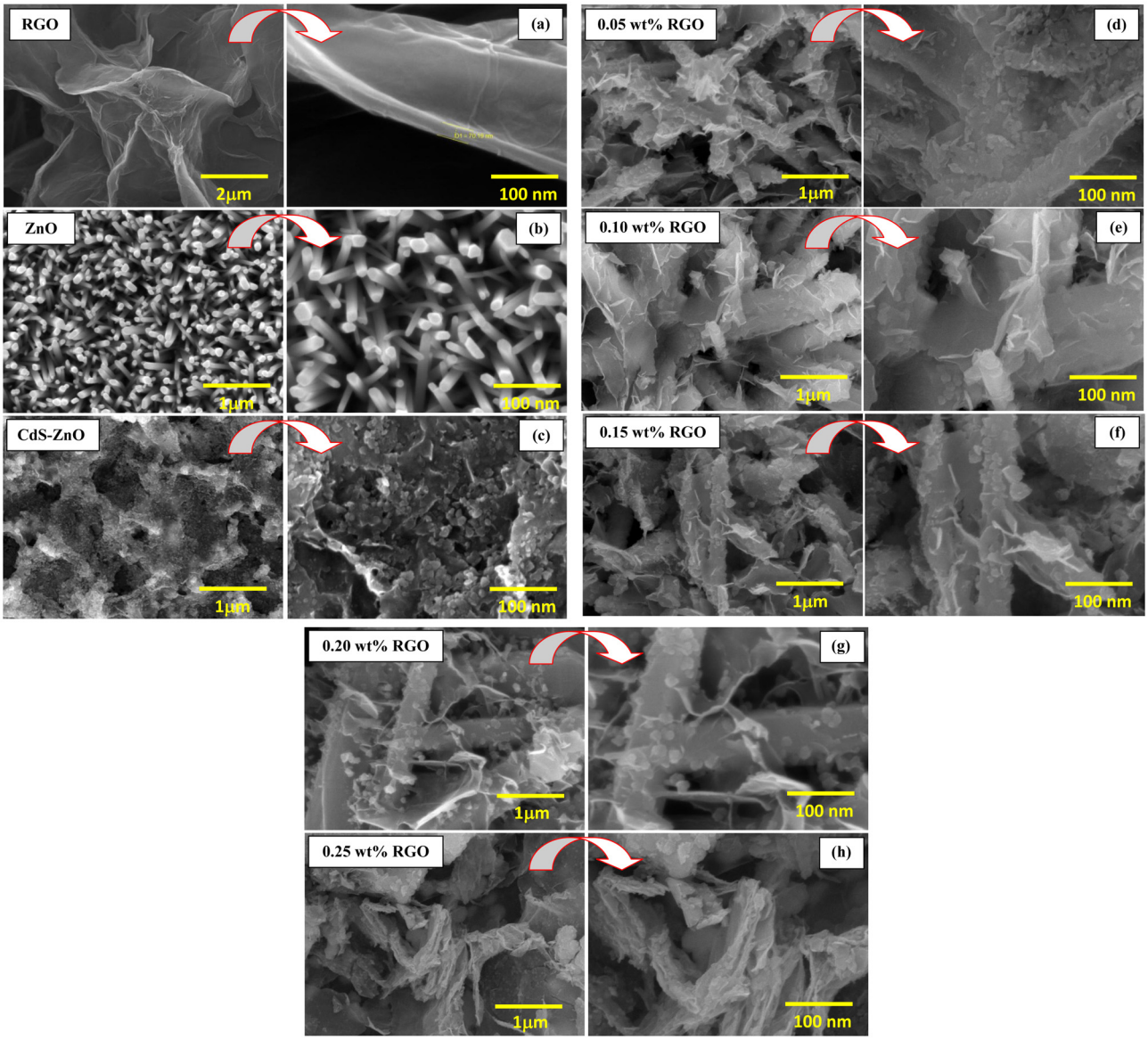

Fig. 2. FE-SEM images of (a) RGO sheets with its size in micrometer at ×50 K and ×150 K, (b) vertically aligned ZnO nanorods at ×50 K and ×150 K, (c) CdS-sensitized ZnO nanorods at ×50 K and ×150 K, (d) RGO- and CdS-sensitized ZnO nanorods with 0.05 wt% of RGO at ×50 K and ×150 K, (e) RGO–CdS–ZnO composite with 0.10 wt% of RGO at ×50 K and ×150 K, (f) RGO–CdS–ZnO composite with 0.15 wt% of RGO at ×50 K and ×150 K, (g) RGO–CdS–ZnO composite with 0.20 wt% of RGO at ×50 K and ×150 K, and (h) RGO–CdS–ZnO composite with 0.25 wt% of RGO at ×50 K and ×150 K.

distilled water. Finally, the washed substrate with film was dried at room temperature for further characterization.

2.4. Characterization

Phase information and crystalline quality of the prepared nanostructures were investigated using X-ray diffraction (XRD; D/MAX-2500/PC, Cu Kα; Rigaku, USA). The surface morphology was studied using a field-emission scanning electron microscope (FE-SEM; JMIRA3 LM; Tescan, USA). The sensitization of the ZnO nanorods by the RGO–CNPs and its elemental analysis were studied by transmission electron microscopy and energy dispersive X-ray analysis (TEM/EDS, JEM-2100F; JEOL, Japan). Electron spectroscopy for chemical analysis (ESCA, sigma probe; ThermoScientific, UK) was done at ultrahigh vacuum using a multichannel electron spectrometer with a spherical sector (180°) electron analyzer (mean radius 275 mm) to confirm the formation of the RGO–CdS–ZnO composite film. Photoluminescence (PL) spectra of deposited RGO–CdS–ZnO films were acquired at room temperature using a fluorescence spectrophotometer (DongWoo Optron, South Korea) with an attached He–Cd laser at an excitation wavelength of 325 nm. Brunauer–Emmett–Teller (BET) specific surface areas of composite films were measured by nitrogen adsorption–desorption (AS-1; Quantachrome Instruments, USA).

2.5. Photocatalytic degradation of methylene blue

The photocatalytic activity of a synthesized nanocomposite was measured by degrading MB (1.0×10^{-5} M, 200 mL) under a halogen lamp (100 W). Sample powder was dispersed (100 mg L^{-1}) in the dye solution while stirring at room temperature for 1 h in the dark to reach adsorption–desorption equilibrium of the photocatalyst. Then, the dye solution containing the dispersed catalyst was illuminated by the halogen lamp (incident powder = 10 mW cm^{-2}) while being continuously stirred. Aliquots (5 mL) of the dye solution were withdrawn at 10-min intervals during the irradiation and

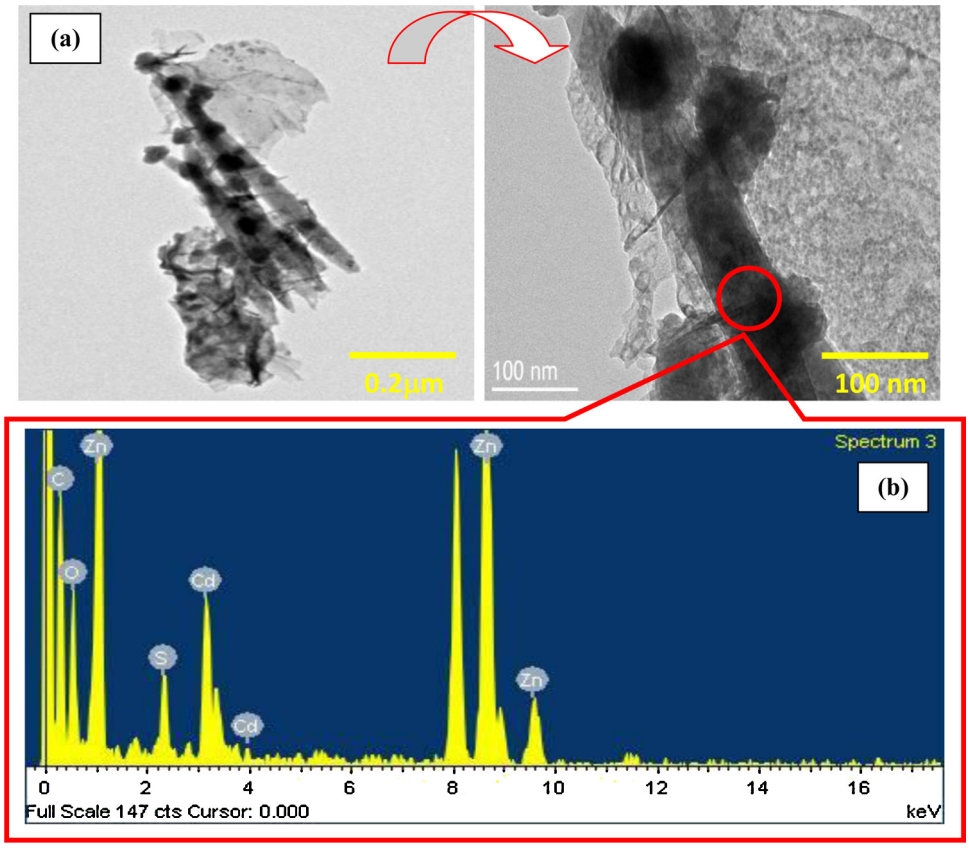

Fig. 3. (a) TEM image of RGO- and CdS-sensitized ZnO nanorods with 0.20 wt% of RGO and its magnified image showing CdS particles attached to ZnO nanorods and (b) EDS spectra of the RGO–CdS–ZnO composite.

analyzed using a UV-VIS spectrophotometer (V-600; Jasco, Japan) after centrifugation. The intensity of the absorption band at 665 nm was monitored to estimate the dye concentration. Control samples consisted of commercial ZnO powders (Junsei Chemical, South Korea) and the catalyst-free MB solution and were measured under the same conditions.

3. Results and discussion

3.1. XRD

Structural features of synthesized RGO powders and RGO–CdS–ZnO composite films with varying amounts of graphene were analyzed by XRD (Fig. 1). The ZnO nanorods film with and without RGO–CdS sensitization had similar diffraction patterns that corresponded to a hexagonal wurtzite crystal structure (JCPDS #01-079-2205). This indicated that the sensitization of graphene and CNPs did not affect the orientation and structure of the ZnO nanorods. The XRD pattern of RGO showed two peaks for the (0 0 2) and (1 0 0) planes (Fig. 1) and confirmed the reduced phase of graphene oxide. However, the absence of RGO and CdS peaks in the composite film was attributable to their much lower intensities compared with that for the ZnO peak. Similar observations have been reported in the literature [37,38].

3.2. FE-SEM

The surface morphologies of RGO, ZnO nanorods, CdS-sensitized ZnO nanorods, and composites of RGO–CdS–ZnO were examined using FESEM as a function of RGO content. RGO sheets several micrometers in size were formed after the reduction of graphene oxide (Fig. 2a). The magnified image shows a thickness of 70 nm, which indicates stacking of graphene sheets. Fig. 3b is a FE-SEM image of ZnO nanorods chemically grown on a glass substrate. The smooth and aligned nanorods grew over the entire substrate and had an average diameter of about 70 nm (magnified image of Fig. 2b). After CdS sensitization, the surface morphology changed significantly (Fig. 2c). The nanorods were completely coated with 30-nm-diameter CNPs; the surface was rougher than that of bare ZnO nanorods. All of the nanorods were covered with CNPs, indicating successful sensitization of the particles (magnified image in Fig. 2c). FE-SEM images of ZnO nanorods sensitized with different amounts of RGO and CNPs are shown in Fig. 2c–g. The RGO and CNPs were deposited together onto the surface of the ZnO nanorods so that the nanorods were completely covered. Wrapping of the nanorods took place as the amount of RGO increased from 0.05 to 0.25 wt%. The number of RGO sheets increased with the addition of 0.25 wt% of RGO to the sample (Fig. 2g). More RGO sheets may improve electron transport while simultaneously lowering the photoelectron recombination rate.

The microstructures of the RGO–CdS–ZnO composites were further studied using TEM (Fig. 3a). It shows that CNPs were distributed over entire RGO sheets as well as they tethered to ZnO nanorods. Further, the magnified TEM image (Fig. 3b) confirms that CNPs (~50 nm) were attached to ZnO nanorods as well as RGO sheets. The elemental composition of an RGO–CdS–ZnO composite was determined using spot energy dispersive X-ray spectroscopy (EDS). The EDS results (Fig. 3c) showed Cd, S, Zn and O, which was consistent with CdS and ZnO being present in the RGO–CdS–ZnO composite.

3.3. XPS

ESCA was used for qualitative analysis of a composite containing reduced graphite oxide sheets, CNPs, and ZnO nanorods. The survey

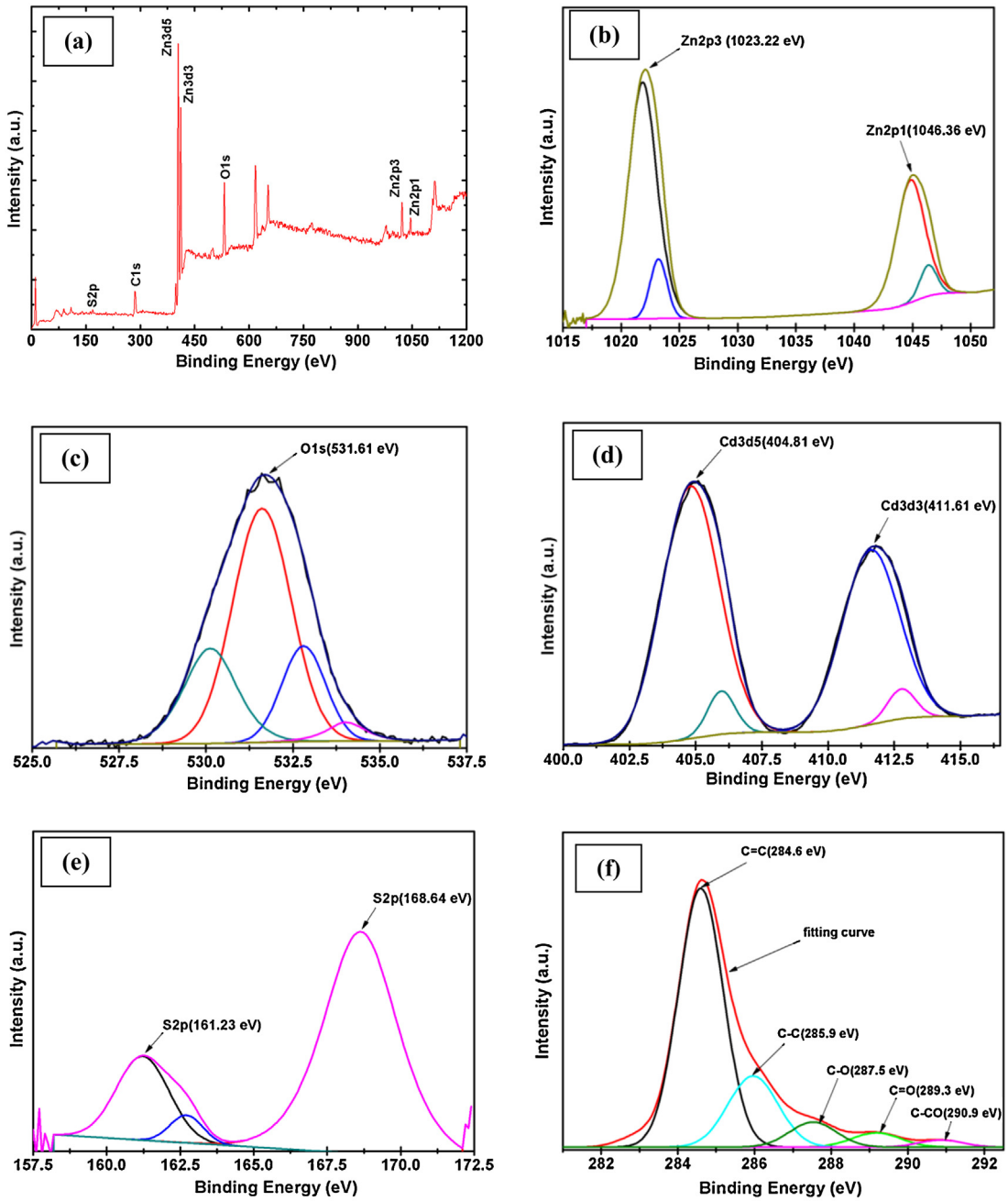

Fig. 4. (a) XPS spectrum of the RGO–CdS–ZnO composite, (b) high-resolution spectrum of the Zn 2p region, (c) high-resolution spectrum of the O 1s region, (d) high-resolution spectrum of the Cd 3d region, (e) high-resolution spectrum of the S 2p region, and (f) high-resolution spectrum of the C 1s region.

spectrum had peaks corresponding to Zn, O, Cd, S, and C, consistent with the formation of a RGO–CdS–ZnO composite (Fig. 4a). Two peaks were observed for the Zn 2p core levels: the one at a binding energy of 1023.22 eV corresponded to Zn $2p^3$ and the other one at 1046.36 eV corresponded to Zn $2p^1$. This indicated that the Zn was present in the form of zinc oxide [39]. The peak corresponding to O 1s was at 531.61 eV (Fig. 4b). The two-peak structure of the Cd 3d core levels derives from a spin–orbit interaction with the Cd $3d^3$ peak at 404.81 eV and the Cd $3d^5$ peak at 411.61 eV [40]. The narrow and well-defined doublet for the Cd 3d structure indicated that the cadmium was present as cadmium sulfide (Fig. 4c) [41]. Similarly, the S peak located at 161.23 eV implied that the sulfur was present as sulfide (Fig. 4d) [42]. The C 1s region had a strong peak centered at 284.6 eV, which corresponded to the C═C group. Additionally C1s spectra exhibited weak peaks at 285.9 eV, 287.5 eV, 289.3 eV and 290.9 eV corresponding to C—C, C—O, C═O and C—CO groups [43–45]. This indicated that the composite contained reduced graphene oxide sheets (Fig. 4e). Hence, the successful formation of the RGO–CdS–ZnO composite was confirmed.

3.4. Absorbance

High optical absorbance is essential for effective photocatalysis. In particular, absorbance in the visible region is important to cover a large portion of the solar spectrum. In the present study, the absorbance spectra of ZnO films with and without RGO–CdS composites were recorded using a UV–VIS spectrophotometer in the range of 350–850 nm. Fig. 5 shows that a significant increase in absorbance in the UV region for ZnO nanorods can be attributed to

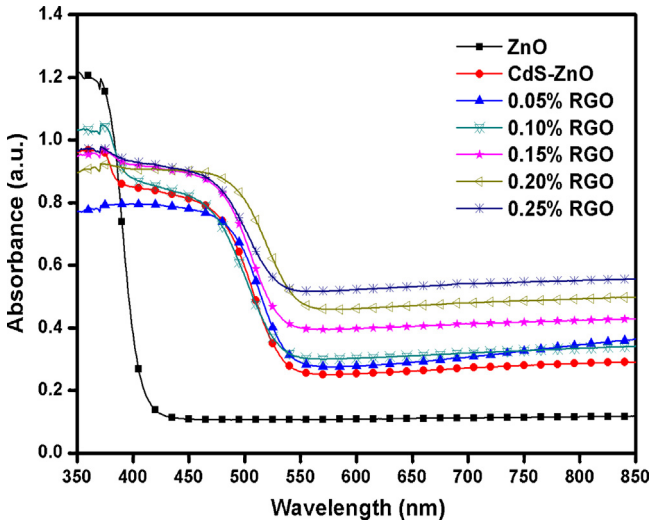

Fig. 5. Optical absorbance spectra of ZnO, CdS–ZnO, and RGO–CdS–ZnO composites.

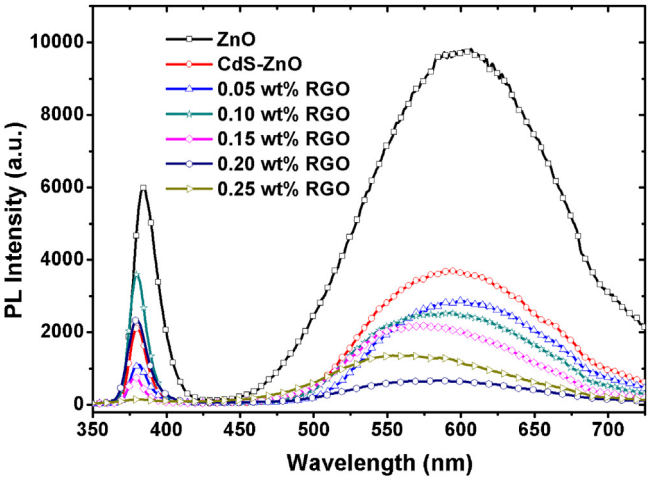

Fig. 6. PPL spectra recorded at room temperature in the range of 350–750 nm with an excitation wavelength of 325 nm for ZnO, CdS–ZnO, and RGO–CdS–ZnO composites.

intrinsic bandgap energy absorption (3.3 eV). After CdS sensitization, the absorption edge shifts toward the visible region because of the bandgap energy of the CNPs (2.4 eV), and its absorbance in the visible region increased after CdS sensitization compared with a ZnO film. RGO–CdS–ZnO films with increasing RGO content showed further increments in UV as well as visible absorbances, while the absorption edge remained at a similar position. Among them, the composite with 0.25 wt% of graphene had the highest absorbance in the visible region. This indicated that the surfaces of the ZnO nanorods were successfully sensitized by the RGO and CNPs. The enhanced absorbance of composites with increasing RGO content indicated the contribution of RGO to the absorbance. These results agree with data reported elsewhere [46,47]. Finally, the increased absorbance in UV and visible regions will improve light harvesting capacity and should enhance the photocatalytic performance of composite samples compared with those made with only CNPs and ZnO nanorods.

3.5. Photoluminescence

Faster electron transfer from the conduction band of the metal oxide to RGO can minimize the recombination rate. The PL spectra (Fig. 6) have both UV and VIS emission peaks. The UV peak (~381 nm) was attributed to near-band-edge transition processes arising from energy loss due to strong electron–phonon interactions at room temperature [48]. The visible peak (~600 nm) was present in all samples but changed in intensity. The high intensity of the visible peak for the ZnO nanorods (~10,000) indicated a high recombination rate. However, the rate decreased with sensitization by CNPs and RGO sheets, and was found to be the lowest for the composite with 0.25 wt% RGO (~1000). This tenfold lower intensity indicated that PL quenching by the RGO had occurred, which would reduce the recombination rate [49]. Therefore, RGO incorporation was expected to increase the photocatalytic degradation rate.

3.6. BET (Brunauer–Emmett–Teller) surface area

The specific surface areas (Table 1) of the synthesized CdS–ZnO and RGO composites were obtained using a nitrogen adsorption–desorption process. RGO addition increased the surface area compared with a CdS–ZnO sample, and it continuously increased with increasing graphene loading. The highest specific area of 23.08 $m^2\ g^{-1}$ was found for the composite with 0.25 wt% of RGO. Hence, RGO increased the surface area of CdS–ZnO samples, a property useful for the adsorption of dye molecules to improve photodegradation.

3.7. Photocatalytic performance

The photocatalytic activities toward MB under visible illumination were evaluated under the same experimental conditions for the synthesized RGO–CdS–ZnO composites. The photocatalytic performance of MB without the catalyst was also measured as a control. Fig. 7 shows that degradation of MB was minimal for the CdS-sensitized ZnO sample. In the presence of CdS–ZnO, MB did not degrade significantly until 40 min of degradation time. However, the RGO–CdS–ZnO composites improved the performance: MB degraded almost completely within 40 min in the presence of the 0.20 wt% RGO–CdS–ZnO composite. The relative variation in absorbance of the MB solution with respect to time in the presence of different photocatalysts under visible light illumination is shown in Fig. 8; the relative absorbance is $100^{*}A_0/A$, where A is the absorbance of the MB solution at illumination time t, and A_0 is the absorbance of the solution before irradiation ($t = 0$). Irradiation by visible light in the absence of catalyst caused a slight decrease in the MB concentration. However, photodegradation of MB occurred significantly after its addition to CdS–ZnO powders and to different RGO–CdS–ZnO composites. The photodegradation rate of the composite with 0.20 wt% RGO was higher than those observed for the other composite samples. Therefore, these differences in degradation rate indicated that the photodegradation depended on the percentage of RGO in the composite sample.

The data in Fig. 8 were also interpreted using the equation $\ln(A_0/A) = -kt$, where A_0/A is the normalized absorbance of the MB

Table 1
Measured specific surface areas ($m^2\ g^{-1}$) and reaction rate constants (min^{-1}) for ZnO, CdS–ZnO, and RGO–CdS–ZnO samples.

Sample details	Specific surface area ($m^2\ g^{-1}$)	Kinetic rate constant (K) min^{-1}
MB	–	0.001
CdS–ZnO	14.38	0.006
0.05 wt%RGO	14.69	0.012
0.10 wt%RGO	15.15	0.014
0.15 wt%RGO	15.72	0.016
0.20 wt%RGO	16.83	0.028
0.25 wt%RGO	23.08	0.018

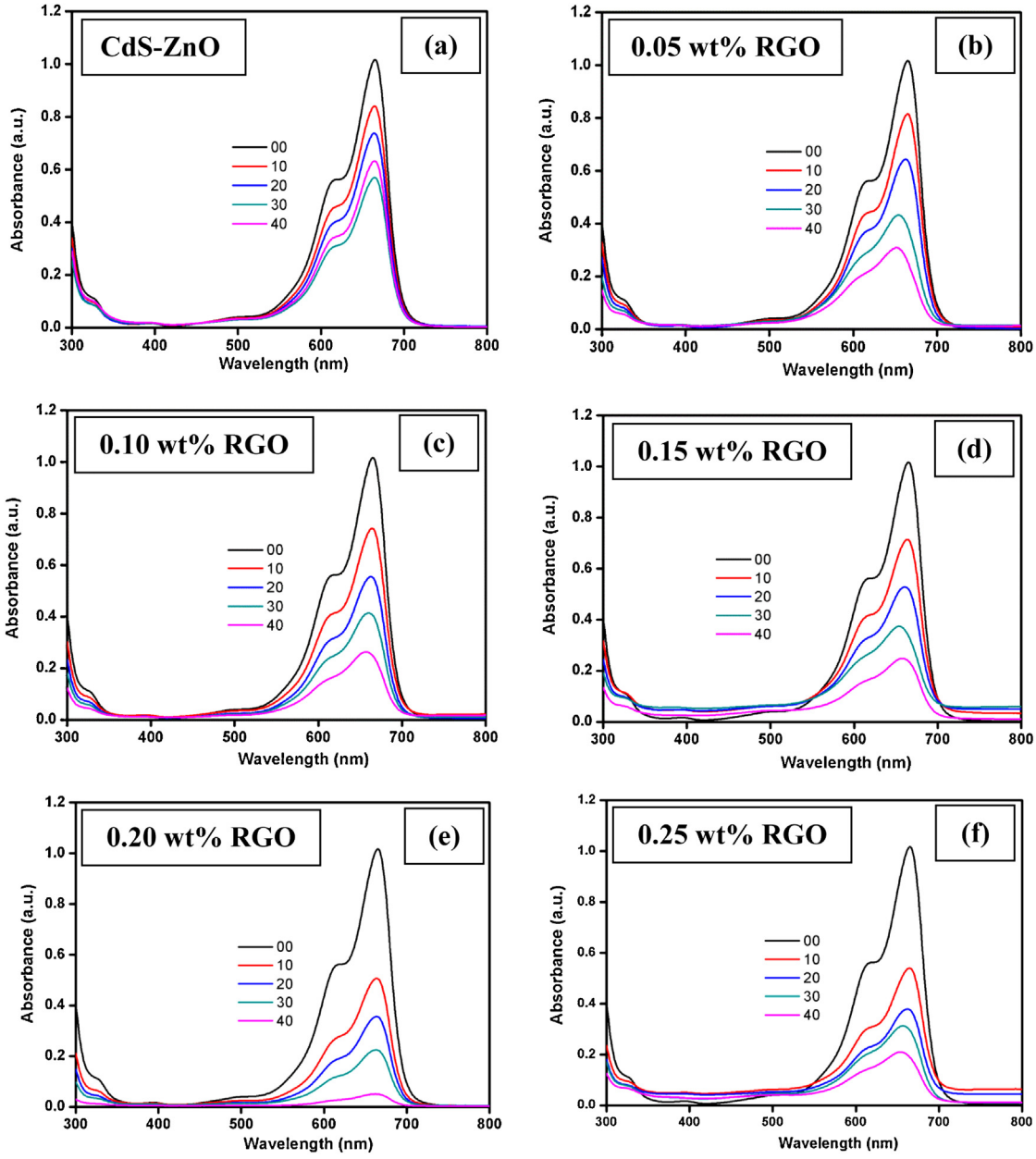

Fig. 7. UV–VIS absorbance spectrums of photocatalytic degradation of MB under visible light using 100 mg L^{-1} of photocatalyst for ZnO, CdS–ZnO, and RGO–CdS–ZnO composites

solution, k is the apparent kinetic rate constant, and t is the reaction time [50]. The linear $\ln(A_0/A)$ vs. t plot (Fig. 9) revealed that the photodegradation of MB followed pseudo-first-order reaction kinetics [51]. The calculated value of k for the 0.20 wt% RGO–CdS–ZnO ($k = 0.028\ min^{-1}$) sample was almost four times higher than that for CdS–ZnO and other composite samples. The k value for the 0.25 wt% RGO–CdS–ZnO sample ($k = 0.018\ min^{-1}$) was slightly higher than that for the 0.05 ($k = 0.012\ min^{-1}$), 0.10 ($k = 0.014\ min^{-1}$), and 0.15 wt% ($k = 0.016\ min^{-1}$) samples, but was lower than that for the 0.20 wt% sample (Table 1). Hence, the RGO–CdS–ZnO composite containing 0.20 wt% RGO had better photocatalytic performance than the samples synthesized with different percentages of RGO and without RGO. Photodegradation performance mainly depends on photoelectron separation before recombination and rapid transport. The improved catalytic performance found for the 0.20 wt% RGO–CdS–ZnO sample is the result of their effective separation and transport because of a PL quenching effect, increased optical absorbance, and specific surface area. However, the photocatalytic performance deteriorated beyond the optimum amount of RGO. Similar behavior has been reported in the literature [52] and can be attributed to the wrapping of CdS and ZnO nanorods by RGO sheets, so that large amount of sheets may act as recombination centers [53,54].

3.8. Possible electron transport mechanism

The enhanced photocatalytic activities of the RGO–CdS–ZnO composites stem from suitable energy band positions of RGO (−4.42 eV), ZnO (−4.21 eV), and CdS (−3.98 eV) (Fig. 10). This improved photoelectron transfer and the high electron mobility of graphene transferred the injected electrons quickly from the interface to the sheets, minimizing recombination losses. Hence, photocatalytic activity improved significantly with the addition of

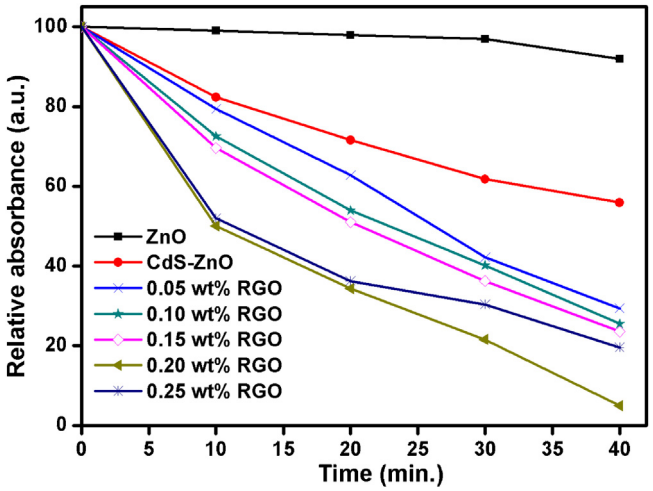

Fig. 8. Relative optical absorbance for CdS–ZnO and RGO–CdS–ZnO composites as a function of irradiation time. The absorbance of the MB solution under visible light irradiation without catalyst is also shown for comparison.

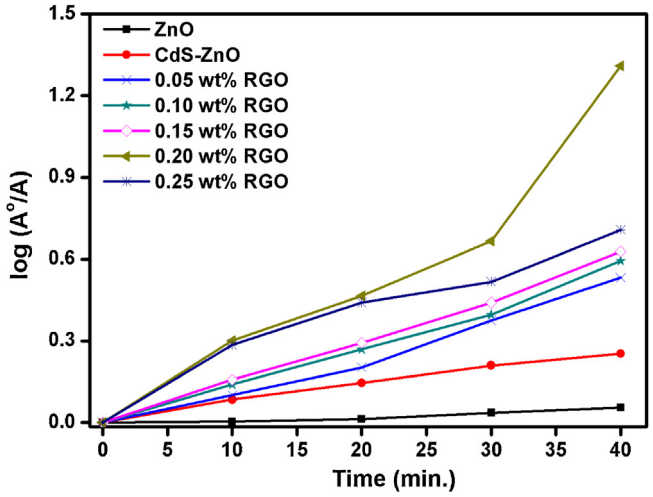

Fig. 9. $\ln(A_0/A)$ vs. t curves for MB photodegradation without catalyst and with ZnO, CdS–ZnO, and RGO–CdS–ZnO catalysts.

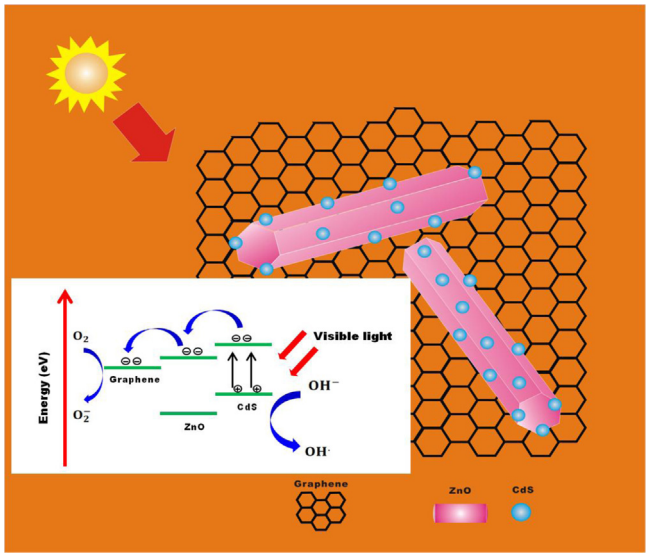

Fig. 10. Schematic diagram of a RGO–CdS–ZnO composite showing the electron transfer mechanism under visible light and photocatalytic degradation of MB dye.

RGO to the CdS–ZnO composite. A proposed series of reaction processes involved in the MB degradation is as follows:

$$\mathrm{CdS} + \mathrm{ZnO} + \text{graphene} \xrightarrow{h\nu} \mathrm{CdS}(h^+_{\mathrm{VE}}) + \mathrm{ZnO}(e^-_{\mathrm{CE}}) + \text{graphene}(e^-) \quad (1)$$

$$\mathrm{CdS}(h^+_{\mathrm{VE}}) + \mathrm{H_2O} \rightarrow \mathrm{CdS} + \mathrm{OH^{\cdot}} \quad (2)$$

$$\text{graphene}(e^-) + \mathrm{O_2} \rightarrow \text{graphene} + \mathrm{O_2^-} \quad (3)$$

$$\cdot\mathrm{O_2^-} + \mathrm{HO_2^{\cdot}} + \mathrm{H^+} \rightarrow \mathrm{H_2O_2} + \mathrm{O_2} \quad (4)$$

$$\mathrm{H_2O_2} + \cdot\mathrm{O_2^-} \rightarrow \cdot\mathrm{OH} + \mathrm{OH^-} + \mathrm{O_2} \quad (5)$$

$$\mathrm{H_2O_2} + e^-_{\mathrm{CB}} \rightarrow \cdot\mathrm{OH} + \mathrm{OH^-} \quad (6)$$

Electron-hole pairs are generated under visible light illumination with an energy ≥2.42 eV. Photogenerated electrons are then transferred toward the ZnO conduction band and to RGO sheets (Eq. (1)). The holes in CdS (h^+_{VB}) generate OH· radicals (Eq. (2)). The electrons captured on the RGO react with oxygen to form transient superoxide radicals and superoxide molecules (Eq. (4)). Highly reactive OH radicals form, which mineralize MB molecules as shown in Eqs. (5) and (6). Thus, graphene plays a crucial role in reducing recombination losses and thereby increasing photocatalytic activity.

4. Conclusions

Composites made with RGO–CdS-sensitized ZnO nanorods have been successfully synthesized using a single-step chemical method at low temperature. FE-SEM and TEM analyses showed that the CNPs and ZnO nanorods were uniformly distributed across the surface of the RGO sheets. XPS spectra confirmed the formation of RGO–CdS–ZnO composites. The quenching of the visible emission peak in the room-temperature PL spectra indicated effective separation of photogenerated electron-hole pairs. The RGO played a crucial role in achieving excellent photocatalytic performance of the synthesized composites toward degradation of MB in visible light. The sample containing 0.20 wt% of RGO had the highest kinetic rate constant (0.028 $\mathrm{min^{-1}}$); this was the optimum amount of RGO for fast electron transport. We thus demonstrated that RGO–CdS–ZnO composites can be fabricated using a cost-effective, single-step chemical method.

Acknowledgments

This research was supported by the Basic Science Research Program of the National Research Foundation of Korea (NRF) funded by the Ministry of Education, Science and Technology (2011-0029862), by a Human Resources Development of the Korean Institute of Energy Technology Evaluation and Planning (KETEP) grant funded by the Ministry of Knowledge Economy, Republic of Korea (No. 20124030200130) and by the National Research Foundation of Korea (NRF) grant funded by the Korea government (MEST) (No. 2012047189). The authors thank Dr. C.H. Ahn and Professor H.K. Cho from Sungkyunkwan University for their assistance with the room temperature photoluminescence measurements.

References

[1] A. Fujishimaa, X. Zhanga, D.A. Tryk, International Journal of Hydrogen Energy 32 (2007) 2664–2672.
[2] W.Y. Teoh, J.A. Scott, R. Amal, The Journal of Physical Chemistry Letters 3 (2012) 629–639.
[3] J.H. Sun, S.Y. Dong, Y.K. Wang, S.P. Sun, Journal of Hazardous Materials 172 (2009) 1520–1526.
[4] M.J. Height, S.E. Pratsinis, O. Mekasuwandumrong, P. Praserthdam, Applied Catalysis B: Environmental 63 (2006) 305–312.

[5] G. Kenanakisa, Z. Giannakoudakis, D. Vernardou, C. Savvakis, N. Katsarakis, Catalysis Today 151 (2010) 34–38.
[6] R.C. Pawar, J.S. Shaikh, P.S. Shinde, P.S. Patil, Materials Letters 65 (2011) 2235–2237.
[7] M. Bizarro, A.S. Arzate, I.G. Wilches, J.C. Alonso, A. Ortiz, Catalysis Today 166 (2011) 129–134.
[8] S. Chakrabarti, B. Chaudhuri, S. Bhattacharjee, P. Das, B.K. Dutta, Journal of Hazardous Materials 154 (2008) 230–236.
[9] R. Qiu, D. Zhang, Y. Mob, L. Song, E. Brewer, X. Huang, Y. Xiong, Journal of Hazardous Materials 156 (2008) 80–85.
[10] Q. Wang, B. Geng, S. Wang, Environmental Science Technology 43 (2009) 8968–8973.
[11] S. Cho, J.W. Jang, J.S. Lee, K.H. Lee, Nanoscale 4 (2012) 2066–2071.
[12] P. Kundu, P.A. Deshpande, G. Madras, N. Ravishankar, Journal of Materials Chemistry 21 (2011) 4209–4216.
[13] X. Yan, C. Zou, X. Gao, W. Gao, Journal of Materials Chemistry 22 (2012) 5629–5640.
[14] Z. Han, L. Liao, Y. Wu, H. Pan, S. Shen, J. Chen, Journal of Hazardous Materials 217–218 (2012) 100–106.
[15] Y. Lai, M. Meng, Y. Yu, X. Wang, T. Ding, Applied Catalysis B: Environmental 105 (2011) 335–345.
[16] V. Eskizeybek, F. Sarı, H. Gulceb, A. Gülce, A. Avcı, Applied Catalysis B: Environmental 119–120 (2012) 197–206.
[17] M. Bizarro, Applied Catalysis B: Environmental 97 (2010) 198–203.
[18] N. Udawatte, M. Lee, J. Kim, D. Lee, ACS Applied Materials Interfaces 3 (2011) 4531–4538.
[19] C. Li, J. Zhang, J. Yang, T. Wang, X. Lv, Z. Tang, Applied Catalysis A: General 402 (2011) 80–86.
[20] J.S. Jang, C.J. Yu, S.H. Choi, S.M. Ji, E.S. Kim, J.S. Lee, Journal of Catalysis 254 (2008) 144–155.
[21] I.A. Shkrob, M.C. Sauer, Journal of Physical Chemistry B 108 (2004) 12497–12511.
[22] H.J. Lee, J.H. Yum, H.C. Leventis, S.M. Zakeeruddin, S.A. Haque, P. Chen, S. Seok, M. Grätzel, M.D.K. Nazeeruddin, Journal of Physical Chemistry C 11 (2008) 11600–11608.
[23] L.J. Diguna, Q. Shen, J. Kobayashi, T. Toyoda, Applied Physics Letters 91 (2007) 023116–023118.
[24] A.J. Nozik, Physica E: Low-dimensional Systems and Nanostructures 14 (2002) 115–120.
[25] P.V. Kamat, Journal of Physical Chemistry C 112 (2008) 18737–18753.
[26] I.M. Sero, S. Gimenez, F.F. Santiago, R. Gomez, Q. Shen, T. Toyoda, J. Bisquert, Accounts of Chemical Research 42 (2009) 1848–1857.
[27] S.A. Vanalakar, R.C. Pawar, M.P. Suryawanshi, S.S. Mali, D.S. Dalavi, A.V. Moholkar, K.U. Sim, Y.B. Kown, J.H. Kim, P.S. Patil, Materials Letters 65 (2011) 548–551.
[28] X. Wang, G. Liu, G.Q. Lu, H.M. Cheng, International Journal of Hydrogen Energy 35 (2012) 8199–8205.
[29] B. Li, Y. Wang, Journal of Physics and Chemistry of Solids 72 (2011) 1165–1169.
[30] S. Stankovich, D.A. Dikin, G.H.B. Dommett, K.M. Kohlhaas, E.J. Zimney, E.A. Stach, R.D. Piner, S.T. Nguye, R.S. Ruoff, Nature 442 (2006) 282–286.
[31] X.Y. Zhang, H.P. Li, X.L. Cui, Y. Lin, Journal of Materials Chemistry 20 (2010) 2801–2806.
[32] G. Zhou, D.W. Wang, F. Li, L. Zhang, N. Li, Z.S. Wu, L. Wen, G.Q. Lu, H.M. Cheng, Chemistry of Materials 22 (2010) 5306–5313.
[33] Z. Wang, H. Zhang, N. Li, Z. Shi, Z. Gu, G. Cao, Nano Research 3 (2010) 748–756.
[34] X. An, J.C. Yu, Y. Wang, Y. Hu, X. Yu, G. Zhang, Journal of Materials Chemistry 22 (2012) 8525–8531.
[35] Y. Sun, Q. Wu, G. Shi, Energy Environmental Science 4 (2011) 1113–1132.
[36] S. Stankovich, D.A. Dikin, R.D. Piner, K.A. Kohlhaas, A. Kleinhammes, Y. Jia, Y. Wu, S.T. Nguyen, R.S. Ruoff, Carbon 45 (2007) 1558–1565.
[37] P. Song, X. Zhang, M. Sun, X. Cui, Y. Lin, Nanoscale 4 (2012) 1800–1804.
[38] X. Liu, L. Pan, T. Lv, G. Zhu, Z. Sun, C. Sun, Chemical Communications 47 (2011) 11984–11986.
[39] S.A. Vanalakar, S.S. Mali, R.C. Pawar, N.L. Tarwal, A.V. Moholkar, J.H. Kim, P.S. Patil, Journal of Applied Physics 112 (2012) 044302–044309.
[40] S.A. Vanalakar, S.S. Mali, R.C. Pawar, N.L. Tarwal, A.V. Moholkar, J.A. Kim, Y. Kwon, J.H. Kim, P.S. Patil, Electrochimica Acta 56 (2011) 2762–2768.
[41] J. Chu, X. Li, J. Qi, Crystal Energy Communications 14 (2012) 1881–1884.
[42] P. Zeng, Q. Zhang, T. Peng, X. Zhang, Physical Chemistry Chemical Physics 3 (2011) 21496–21502.
[43] Y. Shao, J. Wang, M. Engelhard, C. Wang, Y. Lin, Journal of Materials Chemistry 20 (2010) 743–748.
[44] A. Benayad, H.J. Shin, H.K. Park, S.M. Yoon, K.K. Kim, M.H. Jin, H.K. Jeong, J.C. Lee, J.Y. Choi, Y.H. Lee, Chemical Physics Letters 475 (2009) 91–95.
[45] P.G. Ren, D.X. Yan, X. Ji, T. Chen, Z.M. Li, Nanotechnology 22 (2011) 055705–55712.
[46] T. Lv, L. Pan, X. Liu, T. Lu, G. Zhu, Z. Sun, C.Q. Sun, Catalysis Science and Technology 2 (2012) 754–758.
[47] P. Zeng, Q. Zhang, T. Peng, X. Zhang, Physical Chemistry Chemical Physics 13 (2011) 21496–21502.
[48] R.C. Pawar, J.S. Shaikh, A.V. Moholkar, S.M. Pawar, J.H. Kim, J.Y. Patil, S.S. Suryavanshi, P.S. Patil, Sensors and Actuators B: Chemical 151 (2010) 212–218.
[49] A.F. Zedan, S. Sappal, S. Moussa, M.S. Shall, Journal of Physical Chemistry C 114 (2010) 19920–19927.
[50] R.C. Pawar, H. Kim, C.S. Lee, Scripta Materialia 68 (2013) 142–145.
[51] J. Mani, H. Sakeek, S. Habouti, M. Dietze, M.E. Souni, Catalysis Science and Technology 2 (2012) 379–385.
[52] X. Liu, L. Pan, T. Lv, T. Lu, G. Zhu, Z. Sun, C. Sun, Catalysis Science and Technology 1 (2011) 1189–1193.
[53] G. Zhu, T. Xu, T.A. Lv, L.K. Pan, Q.F. Zhao, Z. Sun, Journal of Electroanalytical Chemistry 650 (2011) 248–251.
[54] N. Yang, J. Zhai, D. Wang, Y. Chen, L. Jiang, ACS Nano 4 (2010) 887–894.